Identifying the human optic radiation using diffusion imaging and fiber tractography

Anthony J. Sherbondy Department of Electrical Engineering, Stanford University, Stanford, CA, USA

Robert F. Dougherty Department of Psychology, Stanford University, Stanford, CA, USA

Sandy Napel Department of Radiology, Stanford University, Stanford, CA, USA

Brian A. Wandell Department of Psychology, Stanford University, Stanford, CA, USA

Measuring the properties of the white matter pathways from retina to cortex in the living human brain will have many uses for understanding visual performance and guiding clinical treatment. For example, identifying the Meyer's loop portion of the optic radiation (OR) has clinical significance because of the large number of temporal lobe resections. We use diffusion tensor imaging and fiber tractography (DTI-FT) to identify the most likely pathway between the lateral geniculate nucleus (LGN) and the calcarine sulcus in sixteen hemispheres of eight healthy volunteers. Quantitative population comparisons between DTI-FT estimates and published postmortem dissections match with a spatial precision of about 1 mm. The OR can be divided into three bundles that are segmented based on the direction of the fibers as they leave the LGN: Meyer's loop, central, and direct. The longitudinal and radial diffusivities of the three bundles do not differ within the measurement noise; there is a small difference in the radial diffusivity between the right and left hemispheres. We find that the anterior tip of Meyer's loop is 28 ± 3 mm posterior to the temporal pole, and the population range is 1 cm. Hence, it is important to identify the location of this bundle in individual subjects or patients.

Keywords: diffusion imaging, fiber tractography, lateral geniculate nucleus, optic radiation

Citation: Sherbondy, A. J., Dougherty, R. F., Napel, S., & Wandell, B. A. (2008). Identifying the human optic radiation using diffusion imaging and fiber tractography. *Journal of Vision, 8*(10):12, 1–11, http://journalofvision.org/8/10/12/, doi:10.1167/8.10.12.

Introduction

In the early 19th century Louis-Pierre Gratiolet used brain fixation and dissection to identify and describe the optic radiation (OR) (Leuret & Gratiolet, 1839). This important work showed that retinal signals were sent to localized regions of cortex. This measurement supported the theory of functional specialization of sensory processing in the brain, contradicting the popular belief at the time that the cerebrum was equipotent (Schmahmann & Pandya, 2006).

The OR remains an important subject matter for neuroanatomical inquiry. Measuring the properties of the white matter pathways from retina to cortex in the living human brain will have many uses for understanding visual performance and disabilities. In addition, there has been a great deal of interest in documenting the specific path followed by the OR as it emerges from the lateral geniculate nucleus (LGN) and heads to the calcarine fissure in posterior cortex. The interest is due to widely used neurosurgical interventions that involve resection of the anterior temporal lobe (Yasargil, Türe, & Yasargil, 2004). Anterior temporal lobe resections are performed for several reasons, including tumors and lesions (Choi, Rubino, Fernandez-Miranda, Abe, & Rhoton, 2006; Peltier, Travers, Destrieux, & Velut, 2006), arteriovenous malformations (Kikuta et al., 2006; Okada et al., 2007), and epileptic foci (Choi et al., 2006; Ebeling & Reulen, 1988; Krolak-Salmon et al., 2000; Peltier et al., 2006; Powell et al., 2005; Rubino, Rhoton, Tong, & Oliveira, 2005; Sincoff, Tan, & Abdulrauf, 2004; Taoka et al., 2005; Yasargil et al., 2004). A portion of the OR emerges from the LGN and passes into the anterior temporal lobe before looping back to posterior cortex (Figure 1). This region of the OR, called Meyer's loop (Meyer, 1907), carries signals that represent the entire contralateral upper visual field; avoiding damage to Meyer's loop is essential for preserving this portion of the patient's visual field.

The location of Meyer's loop is variable, with its anterior position varying as much as 1 cm between individuals (Ebeling & Reulen, 1988). Thus, identifying its location in individual patients is of significant value in pre-surgical planning. Currently, DTI-FT offers the only

doi: 10.1167/8.10.12 Received May 12, 2008; published December 17, 2008 ISSN 1534-7362

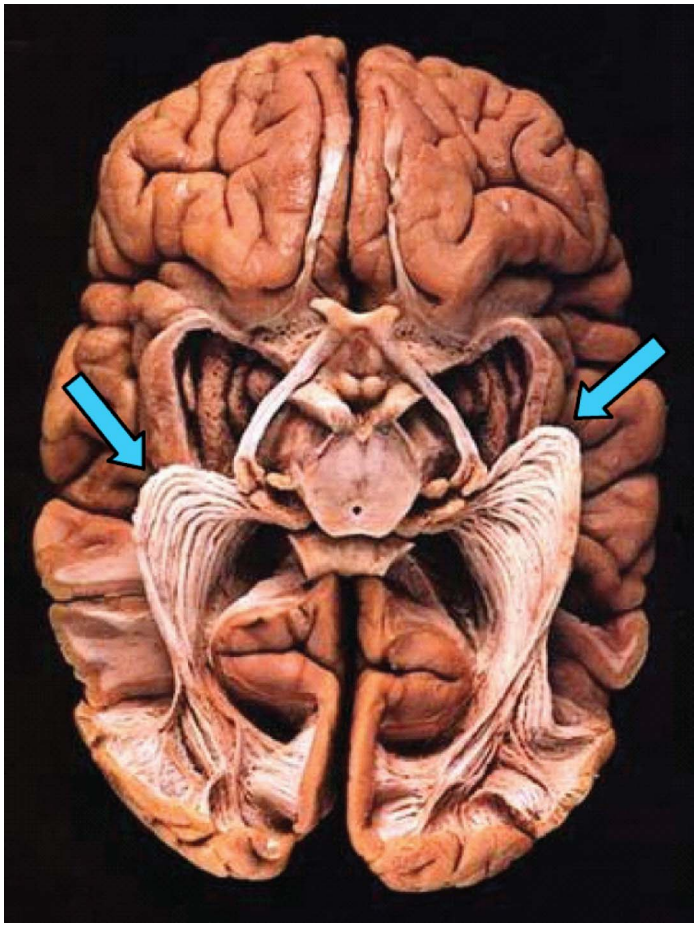

Figure 1. The optic radiation exposed (virtual hospital). A brain, viewed from below, is prepared using Klingler's fiber dissection technique. Meyer's loop, the anterior extension into the temporal lobe, is indicated by the arrows.

non-invasive method for measuring the course of white matter tracts in vivo. The identification of the OR, and in particular the Meyer's loop portion, has received a significant amount of attention from the DTI-FT community (Behrens, Johansen-Berg et al., 2003; Catani, Jones, Donato, & Ffytche, 2003; Ciccarelli et al., 2005; Conturo et al., 1999; Kikuta et al., 2006; Okada et al., 2007; Powell et al., 2005; Taoka et al., 2005; Yamamoto, Yamada, Nishimura, & Kinoshita, 2005). Despite some success, DTI-FT estimates have difficulty identifying the OR and particularly the Meyer's loop section (Miller, 2005; Powell et al., 2005; Yamamoto et al., 2005).

This paper uses the ConTrack algorithm (Sherbondy, Dougherty, Ben-Shachar, Napel, & Wandell, 2008) to identify the OR. This algorithm locates key OR landmarks at positions that match those derived using high-quality dissection methods (Ebeling & Reulen, 1988). Finally, using estimates from a healthy population, we document the longitudinal and radial diffusion characteristics along the entire course of the optic radiation.

Methods

Subjects

Data were obtained from eight healthy subjects with no history of neurological disease, head injury, or psychiatric disorder. The Stanford Panel on Human Subjects in Medical and Non-Medical Research approved all procedures. The eight volunteer subjects (S1: 32y male; S2: 24y male; S3: 27y male; S4: 24y male; S5: 27y male; S6: 23y male; S7: 23y female; S8: 35y male) were recruited from the Stanford University campus. Written informed consent was obtained from all subjects.

Data acquisition

The DTI protocol used 8–10 repetitions of a 90-s whole-brain scan. The scans were averaged to improve signal quality. The pulse sequence was a diffusion-weighted single-shot spin-echo, echo planar imaging sequence (63 msec TE; 6 s TR; 260 mm FOV; 128 × 128 matrix size; ±110 kHz bandwidth; partial *k*-space acquisition). We acquired 48–54 axial, 2-mm-thick slices (no skip) for two *b*-values, $b = 0$ and $b = 800$ s/mm^2. The high *b*-value was obtained by applying gradients along 12 different diffusion directions. Two gradient axes were energized simultaneously to minimize TE and the polarity of the effective diffusion-weighting gradients was reversed for odd repetitions to reduce cross-terms between diffusion gradients and both imaging and background gradients. While Jones (2004) suggests that measuring more diffusion directions might be a more efficient way to reliably estimate diffusion tensors of arbitrary orientation, our signal-to-noise ratio is sufficiently high from our 8–10 repeats to produce very reliable tensor estimates. We have confirmed this in a subset of subjects by comparing bootstrapped tensor uncertainty estimates from 60-direction data with the 12-direction data reported here. With our high SNR, tensor uncertainty is limited by physiological noise rather than measurement noise.

We also collected high-resolution T1-weighted anatomical images for each subject using an 8-minute sagittal 3D-SPGR sequence (1 × 1 × 1 mm voxel size). The following anatomical landmarks were manually defined in the T1 images: the anterior commissure (AC), the posterior commissure (PC), and the mid-sagittal plane. With these landmarks, we used a rigid-body transform to convert the T1-weighted images to the conventional AC–PC aligned space.

Data preprocessing

Eddy current distortions and subject motion in the diffusion-weighted images were removed by a 14-parameter

constrained non-linear co-registration based on the expected pattern of eddy-current distortions given the phase-encode direction of the acquired data (Rohde, Barnett, Basser, Marenco, & Pierpaoli, 2004).

Each diffusion-weighted image was registered to the mean of the (motion-corrected) non-diffusion-weighted ($b = 0$) images using a two-stage coarse-to-fine approach that maximized the normalized mutual information. The mean of the non-diffusion-weighted images was automatically aligned to the T1 image using a rigid body mutual information algorithm. All raw images from the diffusion sequence were resampled to 2-mm isotropic voxels by combining the motion correction, eddy-current correction, and anatomical alignment transforms into one omnibus transform and resampling the data using a 7th-order b-spline algorithm based on code from SPM5 (Friston & Ashburner, 2004).

An eddy-current intensity correction (Rohde et al., 2004) was applied to the diffusion-weighted images at the resampling stage. We note that the 7th-order b-spline interpolation does not require image variance correction (Rohde, Barnett, Basser, & Pierpaoli, 2005) due to the large support kernel. Preserving the signal variance structure in the interpolated data is crucial for an accurate bootstrap variance estimate.

The rotation component of the omnibus coordinate transform was applied to the diffusion-weighting gradient directions to preserve their orientation with respect to the resampled diffusion images. The tensors were then fit using a least-squares algorithm. We confirmed that the DTI and T1 images were aligned to within a few millimeters near the optic radiation. This confirmation was done by manual inspection by one of the authors (RFD). In regions prone to susceptibility artifacts, such as orbito-frontal and inferior temporal regions, the misalignment was somewhat larger due to uncorrected EPI distortions.

All the custom image processing software is available as part of our open-source mrDiffusion package available for download from http://vistalab.stanford.edu/software.

Identification of OR with ConTrack

The ConTrack algorithm can find white matter pathways such as the OR that are known to exist but are difficult for other algorithms to detect (Sherbondy et al., 2008). Similar to other modern probabilistic DTI-FT algorithms, ConTrack can find pathways that are difficult for deterministic DTI-FT techniques because it allows many more possible local pathway orientations for each DTI sample point.

ConTrack improves upon other probabilistic DTI-FT algorithms by separating pathway sampling from pathway scoring and ranking. Specifically, one component of ConTrack, pathway sampling, is designed to search the set of all possible pathways connecting two regions within the DTI data (Figure 2). Another component of ConTrack, pathway scoring, is designed to score the sampled pathways with a function that evaluates the anatomical validity of the pathway by incorporating its fit to the DTI data as well as prior knowledge. Finally, the user sets the lower score threshold for selecting a subset of pathways that estimate the white matter anatomy of interest. This subset can then be used for inferring properties about the connection between the two brain regions. By separating sampling and scoring procedures, the validity of each potential white matter pathway is considered independently.

In the case of the pathways of the OR, previous probabilistic approaches allow the high probability direct connections to mask the presence of the slightly lower probability curved pathways comprising Meyer's loop. This competition reduces the likelihood of observing Meyer's loop (Behrens, Johansen-Berg, et al., 2003; Jbabdi, Woolrich, Andersson, & Behrens, 2007) and makes the loop difficult to discriminate from spurious pathways that are not within the OR (Powell et al., 2005). The independent assignment of validity scores to every pathway connecting the lateral geniculate nucleus (LGN) region of interest (ROI) and the calcarine sulcus ROI allows ConTrack to find the Meyer's loop as well as the higher scoring direct pathways of the OR.

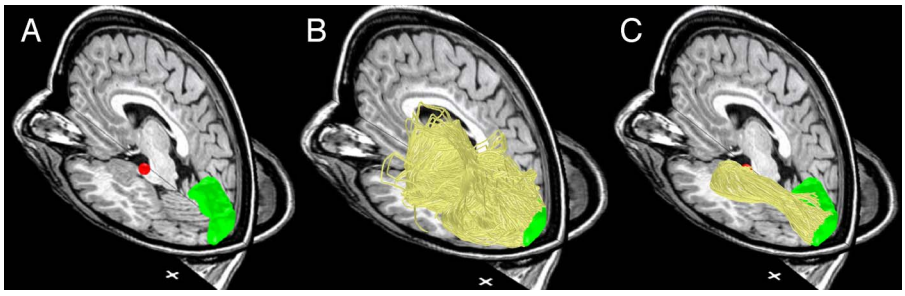

Figure 2. Overview of the ConTrack method for identifying the optic radiation. Co-registered T1 and estimated fiber tracts are shown. (A) LGN (red) and calcarine sulcus (green) ROIs identified by manual segmentation. (B) A large set of potential pathways (yellow) connecting the two ROIs are generated using ConTrack. (C) The top scoring subset is chosen based on a user chosen threshold (Table 1). Cross hairs: 1 × 1 cm (Subject S1).

The ConTrack DTI-FT method is comprised of the following three stages: ROI specification, pathway sampling, and pathway scoring and selection.

ROI specification

The LGN ROI was identified within the DTI data. First, the optic chiasm was located from a fractional anisotropy (FA) map. From this location, one can automatically follow the optic tract from the chiasm to the LGN with a streamlines tracing technique (STT) (Basser, Pajevic, Pierpaoli, Duda, & Aldroubi, 2000; Conturo et al., 1999; Mori, Crain, Chacko, & van Zijl, 1999). We placed a 4-mm radius sphere to cover the STT tracts that reached the most posterior and lateral portion of the thalamus. The size of this ROI (270 mm^3) was chosen to include the entirety of the LGN, which ranges from 91 to 157 mm^3 (Andrews, Halpern, & Purves, 1997). The second ROI was chosen to cover the calcarine sulcus of the occipital lobe. This ROI was manually segmented in each hemisphere from the mean non-diffusion-weighted images using itkSnap (Yushkevich et al., 2006). The higher-resolution T1 images were used to resolve occasional ambiguities in the lower-resolution DTI images.

Pathway sampling

ConTrack's pathway sampling algorithm uses both ROIs as boundaries defining potential starting points and retained only pathways that satisfied the following criteria: pathway length was <300 mm, pathway bending angle for a single step could not exceed 130°, pathways could not step through manually defined regions of gray matter, and pathways had an endpoint within both ROIs. The algorithm was run to collect 100,000 pathway samples between the two ROIs and the pathway step size was set to 1 mm. This required between 50 and 120 minutes of execution time per hemisphere on a single 1 GHz AMD Opteron core with 2 GB of RAM.

Pathway scoring and selection

Many of the 100,000 sampled pathways will be a poor representation of the optic radiation anatomy. The pathways are ordered by a score (Q) that assesses their anatomical validity, where highest scoring is most likely valid. The scoring function combines the pathway fit to the DTI data with prior information on tract smoothness and length. Specifically, the score is divided into two terms. One term evaluates the likelihood of observing the data given the pathway. The second term evaluates the likelihood of the pathway, itself.

To run the scoring algorithm the user must decide on the values of three key parameters. One parameter, η, influences the penalty for a mismatch between the local pathway direction and the principal diffusion direction. This parameter was set to its default value, 0.175. A second parameter, σ_c, influences the penalty for local pathway curvature (Sherbondy et al., 2008). This parameter was set to 14°. The third parameter, λ, influences the preferred pathway length. Because there is considerable range in the length of optic radiation pathways, we set this parameter to a value that does not discriminate between long and short pathways, $\lambda = 1$. The score is the product of local scores for many unit step intervals along a pathway. Again, to avoid a length penalty, we used the geometric mean of these products. More details on ConTrack are provided elsewhere (Sherbondy et al., 2008).

The subset of pathways representing the optic radiation was selected by eliminating pathways with a score below a threshold score (Q_t) that was manually determined for each hemisphere using DTI-Query (Sherbondy, Akers, Mackenzie, Dougherty, & Wandell, 2005). The Q_t value was first set as the highest score of any pathway. Then, Q_t was lowered until three distinct bundles of the OR were

	Threshold (Q_t)		No. of pathways > threshold		Pruned pathways	
ID	L	R	L	R	L	R
S1	0.8	1.2	7352	8016	884 (12%)	44 (0.5%)
S2	1.5	1.5	4498	13791	7 (0.1%)	3 (0.02%)
S3	1.2	1.5	11924	16779	28 (0.2%)	7 (0.04%)
S4	0.5	1.2	2670	5720	642 (24%)	26 (0.4%)
S5	0.8	0.5	47134	13217	0 (0%)	298 (2%)
S6	1.2	0.7	12918	2714	6 (0.04%)	182 (7%)
S7	0.5	1.4	7749	11340	129 (17%)	18 (0.2%)
S8	0.8	1.2	2628	4854	480 (18%)	128 (2.6%)

Table 1. Summary of the optic radiation selection process. The first column contains the score threshold (Q_t). The second column is the number of pathways (out of 100,000) above this threshold. The third column is the number (percentage) of above-threshold pathways that were manually pruned using the method described in the text.

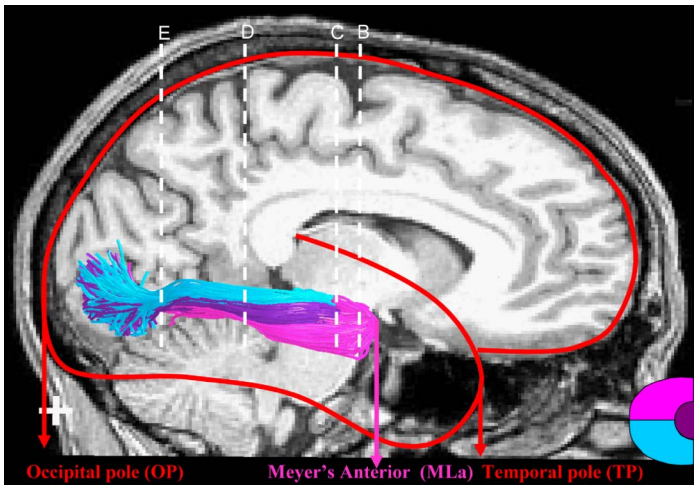

Figure 3. Anatomical coordinates for assessing the optic radiation location, as defined by Ebeling and Reulen (1988). The ConTrack OR estimates are illustrated on the right hemisphere. The background image is a co-registered mid-sagittal T1 image. The red outline of the brain indicates the position of the temporal pole (TP) and the occipital pole (OP). The ConTrack OR estimates are colored according to the direct (blue), central (purple), and Meyer's loop (pink) bundles. These carry information about the lower, foveal, and upper left visual field, respectively (see inset, lower right). The anterior position of Meyer's loop (MLa) is labeled. The white dotted lines (B, C, D, and E) are the locations of the coronal images in Figure 5. Subject S1. Cross hair: 1 × 1 cm.

visualized and only a few pathways remained that deviated significantly from one of the three bundles. Pathways that intersected more than one voxel of visually obvious regions of gray matter or cerebral spinal fluid also were manually removed. This hand editing is necessary because automatic tissue identification algorithms do not provide adequate accuracy. The percentage of discarded pathways compared to the retained subset of OR pathways was generally small (Table 1).

Identification of anatomical landmarks used to position the OR

In order to compare the OR estimated by ConTrack with the results from dissection studies, we identified the following anatomical landmarks: anterior tip of the temporal pole (TP), anterior tip of Meyer's loop (MLa), anterior tip of the temporal horn (TH), and the posterior tip of the occipital pole (OP) (Figure 3). The TP, TH, and OP positions were all identified in each hemisphere using the non-diffusion-weighted image from the diffusion imaging sequence (see above). The position of MLa was determined as the furthest anterior position of pathways identified as Meyer's loop. The OR pathway estimates were manually separated into three distinct bundles. The Meyer's loop was determined to be any pathway that projected in an orientation inferior and anterior from the LGN. The central bundle was determined by selecting any pathway that extended in a lateral direction from the LGN. The direct bundle was defined as any remaining pathway that was neither the Meyer's loop nor the central bundle.

The ConTrack software and documentation is available as an open-source distribution from the Web site (http://www.simtk.org/home/contrack).

Results

Position and course of the OR

The OR was identified in all hemispheres of the 8 healthy subjects (Figure 4). The most anterior position of

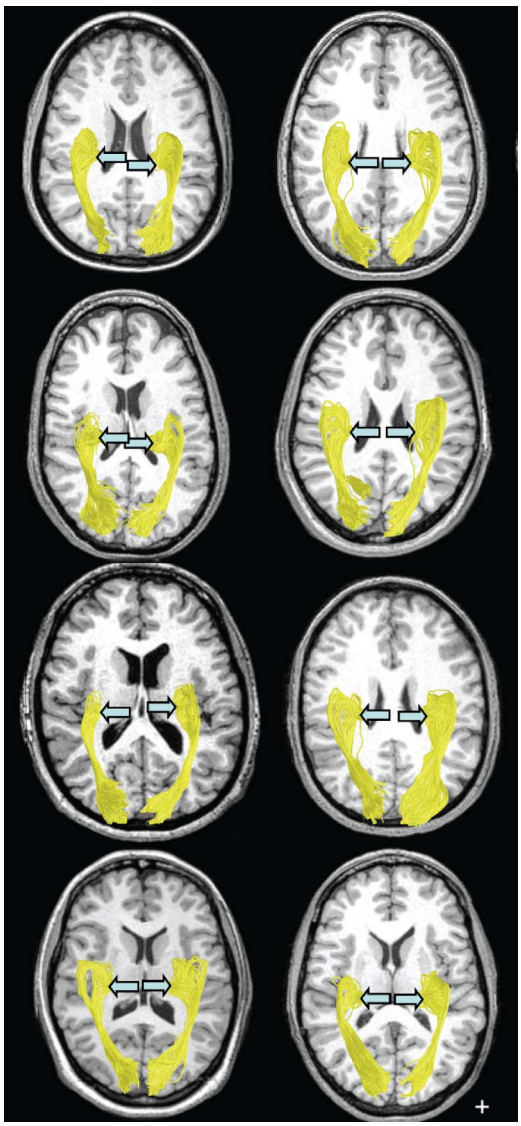

Figure 4. Estimated OR in 16 hemispheres, viewed from below. The position of the LGN (blue arrow) is indicated for each hemisphere. Cross hair: 1 × 1 cm.

the Meyer's loop was found to be an average distance of 28 mm from the temporal pole, in agreement with the dissection results of Ebeling and Reulen (1988). Furthermore, the measurements of the distance between the anterior location of the Meyer's loop and the occipital pole as well as the location of this point of the OR with respect to the tip of the temporal horn agree quite well with the dissection results (see Discussion).

To verify that our measurements were robust to outliers, we also measured the most anterior position after excluding the 5% of fibers in Meyer's loop closest to the temporal pole. The average position of this measurement differed from the reported position by only 2 mm.

In addition to the distance measurements of the position of the OR with respect to anatomical landmarks, we also examined the course of the OR along a sequence of coronal sections. In Figure 5, one representative subject (S1) demonstrates the correspondence between ConTrack's estimation of the OR and the dissected fibers of Ebeling and Reulen (1988). By visual inspection, the ordering (topological) relationship between the central, direct, and Meyer's bundles along the course of the OR matches the illustrations reproduced from Ebeling and Reulen.

Diffusivity within the OR

To characterize the diffusion properties of the OR, we computed the longitudinal and radial diffusivity values for the separate OR bundles (Meyer's, Central, Direct) and for all of the white matter (All). Longitudinal diffusivity is the largest eigenvalue of the diffusion tensor, and radial diffusivity is the mean of the remaining two eigenvalues.

To identify voxels within the core of the optic radiation and the white matter, we considered only voxels with a linearity index (C_L) greater than 0.3 (see Figure 6). Linearity measures anisotropy; it is the positive difference between the largest two eigenvalues of the diffusion tensor divided by the sum of its eigenvalues (Peled, Gudbjartsson, Westin, Kikinis, & Jolesz, 1998). We previously described how this value may be used to indicate how likely the DTI signal is a measurement from one fascicle orientation (Sherbondy et al., 2008). The linearity values select diffusion data along the pathways that are more likely to be within the core of the OR and less corrupted by partial voluming with CSF, gray matter, or crossing fiber tracts.

For each hemisphere, we estimated 4 mean longitudinal diffusivity values and 4 mean radial diffusivity values (Meyer's, Central, Direct, All). Mean ± SE longitudinal diffusivities (in units of μm^2/msec) were 1.56 ± 0.01, 1.57 ± 0.01, 1.57 ± 0.01, and 1.49 ± 0.01 for the four groups, respectively. Mean ± SE radial diffusivities were 0.448 ± 0.006, 0.445 ± 0.007, 0.442 ± 0.008, and 0.414 ± 0.005 μm^2/msec, respectively.

The only significant difference between the diffusivity measures was between the (All) group and each of the OR groups ($p < 0.01$, two-sample t-test). We also averaged the three optic radiation bundles and compared the left and

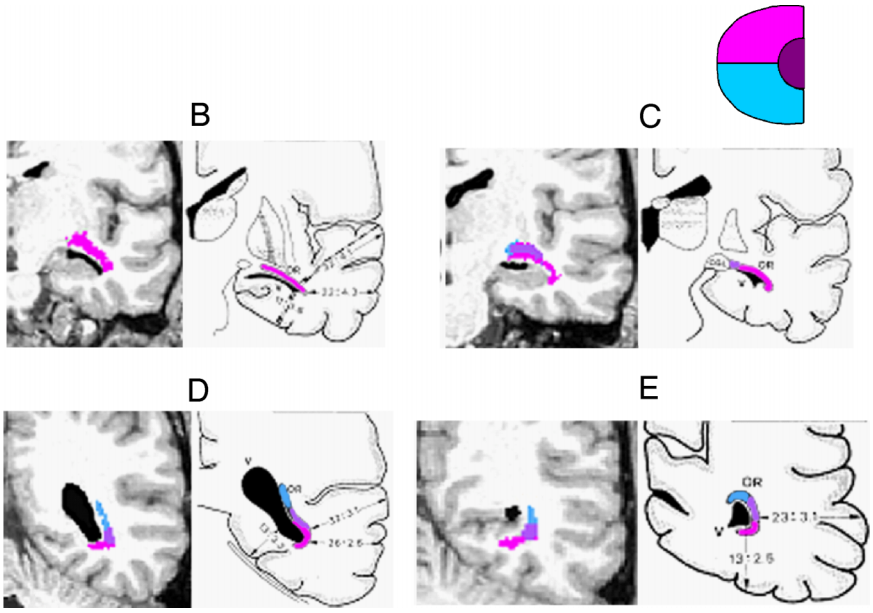

Figure 5. Coronal sections showing the position of the direct, central, and Meyer's loop bundles within the OR. Each panel compares an MR image and estimated fibers (left) with illustrations from a dissection study (Ebeling & Reulen, 1988) (right). The positions of the OR bundles are shown by the color overlays, and the expected visual information carried by these bundles is indicated by the inset (upper right). The locations of the coronal slices (B, C, D, and E) are shown in Figure 3. Subject S1.

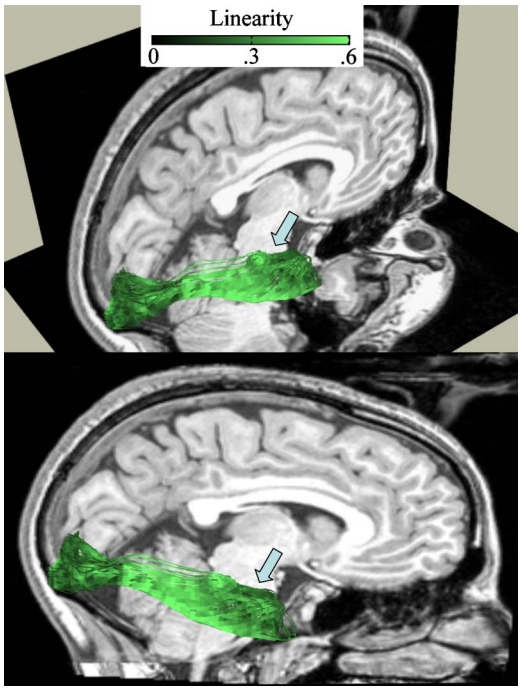

Figure 6. Linearity index along the OR. The linearity index is sampled at 1-millimeter arc length. The linearity index value is shown by the inset. The T1-weighted background image is a sagittal right hemisphere slice, near the bottom of the calcarine sulcus. The two images show the same data from different viewpoints. Subject S2.

right OR diffusivities (Figure 7). The radial diffusivities are systematically higher in the right compared to the left hemisphere.

Discussion

A series of neurological reports discuss the disruption of the visual field following resection of the anterior temporal lobe. Hughes et al. (1999) observed that nearly every patient they measured showed a visual field loss when measured using automated static perimetry (Humphrey visual fields). They note that these patients were not aware of this loss; it was only revealed by formal testing. Roughly half of the patients lost visual field sensitivity within 9 deg of the fovea, and a quarter of the patients lost visual field within 3 deg of the fovea.

Krolak-Salmon et al. (2000) report that 15 of 18 patients presented with a post-operative visual field loss. They report two cases in which the resection was limited to 20 mm from the temporal pole but still produced a partial quadrantanopia.

In both Hughes et al. (1999) and Krolak-Salmon et al. (2000), the post-operative visual field loss was in the upper visual field, consistent with our understanding of the information carried on the anterior portion of Meyer's loop. Hence, these reports suggest that the resection specifically damages the anterior portion of Meyer's loop, which typically is located near the temporal horn.

Population statistics from anatomical measurements are used to guide tissue resection (Choi et al., 2006; Ebeling & Reulen, 1988; Peltier et al., 2006; Rubino et al., 2005; Sincoff et al., 2004; Yasargil et al., 2004). But there is considerable individual variability in the precise position of the anterior portion of Meyer's loop, as reported in (Ebeling & Reulen, 1988) and in our results here. Hence, it is probably not practical to identify a single fixed position as a safe limit for resection. The individual variability makes it greatly preferable to identify the location of Meyer's loop in each patient.

Related literature

We compare various estimates of the position of Meyer's loop in Table 2. The table shows the position of the anterior portion of Meyer's loop (MLa) with respect to several anatomical landmarks (see Figure 3).

The gold standard for pre-operative detection of the course of the OR is based on the gross dissection technique on frozen, formalin fixed tissue (Klingler method) (Ebeling & Reulen, 1988). These estimates, shown in the first data column, agree very closely with the ConTrack estimates (second data column). The Ebeling and Reulen (1988) study is also used as the gold standard for OR location measurements in two previous

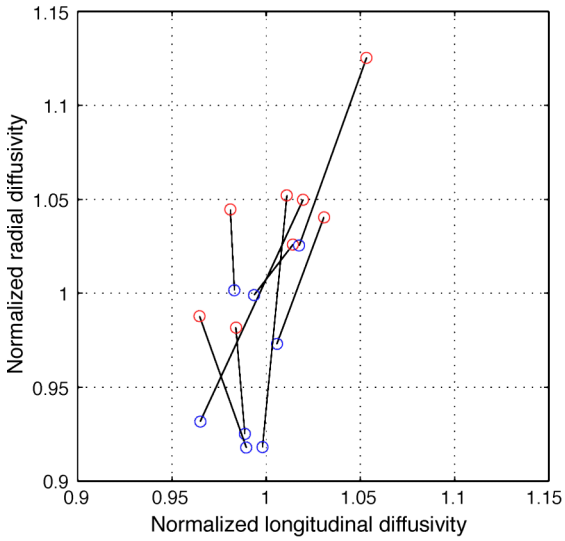

Figure 7. Scatter plot of radial and longitudinal diffusivity comparing left (blue) and right (red) hemispheres. Points from individual subjects are connected by a line. The radial diffusivity is approximately 7% higher, on average, in the right hemisphere. Only voxels with a linearity index above 0.3 are included in the calculation. The axes are normalized to the mean longitudinal (1.57 μm^2/msec) or radial (0.45 μm^2/msec) diffusivity.

Measurement	Dissection (Ebeling & Reulen, 1988), $X \pm SD$ min–max (mm)	ConTrack (Sherbondy et al., 2008), $X \pm SD$ min–max (mm)	STT (Yamamoto et al., 2005), $X \pm SD$ min–max (mm)	STT (Nilsson et al., 2007), $X \pm SD$ min–max (mm)
MLa–TP	27 ± 3.5	28 ± 3.0	37 ± 2.5	44 ± 4.9
(distance)	22 – 37	24 – 34	33 – 40	34 – 51
MLa–OP	98 ± 6.2	96 ± 5.5	82 ± 3.0	NA
(distance)	85 – 108	89 – 108	77 – 85	
MLa–TH	5 ± 3.2	3 ± 2.6	−4 ± 0.2	−15 ± 4
(position)	−5 to 10	−1 to 8	−4.3 to −3.7	−21 to −8

Table 2. Distance between the anterior position of Meyer's loop (MLa) and other anatomical landmarks. The rows indicate the distance between the MLa and (1) the temporal pole (TP), (2) the occipital pole (OP), and (3) the temporal horn (TH); anterior is positive relative to the TH. The four data columns are estimates from Ebeling and Reulen (1988), ConTrack, Yamamoto et al. (2005), and Nilsson et al. (2007). Measurements by Ebeling and Reulen and ConTrack (columns 1 and 2) are in good agreement. The mean position of the MLa, as measured by Yamamoto et al. and Nilsson et al. (columns 3 and 4), differ from Ebeling and Reulen by more than 1 cm, posterior.

DTI-FT methods (Nilsson et al., 2007; Yamamoto et al., 2005) and the data have been confirmed by additional dissection (Choi et al., 2006; Peltier et al., 2006; Rubino et al., 2005) and clinical studies (Hughes et al., 1999; Krolak-Salmon et al., 2000).

Two previous measurements of the OR position based on STT methods are shown in the third and fourth data columns (Nilsson et al., 2007; Yamamoto et al., 2005). These authors estimate the mean anterior position of Meyer's loop to be at least 1 cm posterior to estimates from dissection studies (Ebeling & Reulen, 1988).

For example, Nilsson et al. (2007) find the temporal horn 1.5 cm anterior to Meyer's loop. They suggest that the discrepancy may be due to mis-identification of the fibers during dissection or errors in the dissection estimates of absolute distances. Distance errors are not an adequate explanation because the anatomical descriptions also include ordering information. For example, Sincoff et al. (2004) writes: "The anterior tip of the temporal horn was covered by the anterior optic radiation along its lateral half (abstract)." Choi et al. (2006) writes: "In all of our specimens, the anterior edge of the Meyer's loop reached the tip of the temporal horn (p. 232; see also Figure 3 in that article)." Forced to choose between DFT estimates and anatomical dissection at this point in time, we think anatomists should have priority.

The high false-negative (miss) rate of the STT algorithms has been reported in the literature, and there has been much progress on new algorithms designed to address this issue. Specifically, probabilistic methods have been developed to address the uncertainty within the diffusion data and locate valid pathways previously hidden to STT (Anwander, Tittgemeyer, von Cramon, Friederici, & Knösche, 2007; Behrens, Woolrich, et al., 2003; Bjornemo, Brun, Kikinis, & Westin, 2002; Friman & Westin, 2005; Hagmann et al., 2003; Hosey, Williams, & Ansorge, 2005; Lazar & Alexander, 2002; Parker, Haroon, & Wheeler-Kingshott, 2003; Perrin et al., 2005). As we have previously reported, many of these new techniques also fail to identify valid white matter pathways. Elsewhere, we specifically considered the problem these algorithms have with identifying the optic radiation and Meyer's loop (Sherbondy et al., 2008).

Despite the known limits of STT algorithms, their computational simplicity and ease of interpretation are very attractive for clinical applications. Thus, several groups have applied STT to identify Meyer's loop and predict the visual consequences of temporal lobe resections and disease (Kikuta et al., 2006; Okada et al., 2007; Yamamoto et al., 2007; Yamamoto et al., 2005). To identify Meyer's loop with STT (e.g., FACT), investigators use the following approach. First, they use a brute force approach for identifying a large set of fibers within each hemisphere. The threshold for terminating a fiber path, in particular the threshold for the turn angle, is set to a liberal value. They then identify a series of regions of interest at the locations that are characteristic of the optic radiation, including the Meyer's loop position and regions near the LGN and calcarine cortex. The fibers that fall within these regions, and not other identifiable regions, are the estimated OR fibers.

Okada et al. (2007) used this method to identify the OR in patients with arteriovenous malformations (AVMs). In a series of patients, they observed a correlation between visual field loss and the ability to identify intact optic radiation fibers. Using a similar approach, Kikuta et al. (2006) report a similar correlation between visual performance and the ability to track OR fibers. Neither group assessed whether the position of the estimated OR matched controls because neither group studied normal controls. Finally, even without tractography, Taoka et al. (2005) showed that basic diffusion properties, such as fractional anisotropy within manually segmented optic radiation, was a useful predictor of visual performance.

These studies illustrate that diffusion-weighted imaging and tractography contains a great deal of useful information about the optic radiation and that these measures relate to visual performance. The Yamamoto et al. (2005) study shows that the STT approach to identifying these pathways gives a first approximation but does not match

the gold standard identified in dissection studies (Ebeling & Reulen, 1988).

The ConTrack method improves the estimation precision for the optic radiation considerably. Specifically, ConTrack estimates reduce the error from a centimeter or more in STT methods to within the error rate of the dissection method (millimeters). This increased precision should provide us with better guidance during surgical procedures, and it should also enable visual neuroscientists to measure the position and properties of the optic radiation accurately.

Acknowledgments

The authors thank Dr. P. Basser for discussion of the ConTrack algorithm, Dr. N. Imbar for help in optic radiation analysis, and Dr. R. Bammer for data acquisition assistance. Supported by NIH EY015000.

Commercial relationships: none.
Corresponding author: Anthony Sherbondy.
Email: sherbond@stanford.edu.
Address: 450 Serra Mall, Room 490, Jordan Hall, Stanford, CA 94305, USA.

References

Andrews, T. J., Halpern, S. D., & Purves, D. (1997). Correlated size variations in human visual cortex, lateral geniculate nucleus, and optic tract. *Journal of Neuroscience, 17,* 2859–2868. [PubMed] [Article]

Anwander, A., Tittgemeyer, M., von Cramon, D. Y., Friederici, A. D., & Knösche, T. R. (2007). Connectivity-based parcellation of Broca's area. *Cerebral Cortex, 17,* 816–825. [PubMed] [Article]

Basser, P. J., Pajevic, S., Pierpaoli, C., Duda, J., & Aldroubi, A. (2000). In vivo fiber tractography using DT-MRI data. *Magnetic Resonance in Medicine, 44,* 625–632. [PubMed]

Behrens, T. E., Johansen-Berg, H., Woolrich, M. W., Smith, S. M., Wheeler-Kingshott, C. A., Boulby, P. A., et al. (2003). Non-invasive mapping of connections between human thalamus and cortex using diffusion imaging. *Nature Neuroscience, 6,* 750–757. [PubMed]

Behrens, T. E., Woolrich, M. W., Jenkinson, M., Johansen-Berg, H., Nunes, R. G., Clare, S., et al. (2003). Characterization and propagation of uncertainty in diffusion-weighted MR imaging. *Magnetic Resonance in Medicine, 50,* 1077–1088. [PubMed]

Bjornemo, M., Brun, A., Kikinis, R., & Westin, C. (2002). *Regularized stochastic white matter tractography using diffusion tensor MRI*. Paper presented at the MICCAI.

Catani, M., Jones, D. K., Donato, R., & Ffytche, D. H. (2003). Occipito-temporal connections in the human brain. *Brain, 126,* 2093–2107. [PubMed] [Article]

Choi, C., Rubino, P. A., Fernandez-Miranda, J. C., Abe, H., & Rhoton, A. L., Jr. (2006). Meyer's loop and the optic radiations in the transsylvian approach to the mediobasal temporal lobe. *Neurosurgery, 59,* 228–235. [PubMed]

Ciccarelli, O., Toosy, A. T., Hickman, S. J., Parker, G. J., Wheeler-Kingshott, C. A., Miller, D. H., et al. (2005). Optic radiation changes after optic neuritis detected by tractography-based group mapping. *Human Brain Mapping, 25,* 308–316. [PubMed]

Conturo, T. E., Lori, N. F., Cull, T. S., Akbudak, E., Snyder, A. Z., Shimony, J. S., et al. (1999). Tracking neuronal fiber pathways in the living human brain. *Proceedings of the National Academy of Sciences of the United States of America, 96,* 10422–10427. [PubMed] [Article]

Ebeling, U., & Reulen, H. J. (1988). Neurosurgical topography of the optic radiation in the temporal lobe. *Acta Neurochirurgica, 92,* 29–36. [PubMed]

Friman, O., & Westin, C. F. (2005). Uncertainty in white matter fiber tractography. In *Proceedings of the Medical Image Computing and Computer-Assisted Intervention, 8,* 107–114. [PubMed]

Friston, K., & Ashburner, J. (2004). *Statistical parametric mapping*. Retrieved from http://www.fil.ion.ucl.ac.uk/spm/software/spm2/.

Hagmann, P., Thiran, J. P., Jonasson, L., Vandergheynst, P., Clarke, S., Maeder, P., et al. (2003). DTI mapping of human brain connectivity: Statistical fibre tracking and virtual dissection. *Neuroimage, 19,* 545–554. [PubMed]

Hosey, T., Williams, G., & Ansorge, R. (2005). Inference of multiple fiber orientations in high angular resolution diffusion imaging. *Magnetic Resonance in Medicine, 54,* 1480–1489. [PubMed]

Hughes, T. S., Abou-Khalil, B., Lavin, P. J., Fakhoury, T., Blumenkopf, B., & Donahue, S. P. (1999). Visual field defects after temporal lobe resection: A prospective quantitative analysis. *Neurology, 53,* 167–172. [PubMed]

Jbabdi, S., Woolrich, M. W., Andersson, J. L., & Behrens, T. E. (2007). A Bayesian framework for global tractography. *Neuroimage, 37,* 116–129. [PubMed]

Jones, D. K. (2004). The effect of gradient sampling schemes on measures derived from diffusion tensor MRI: A Monte Carlo study. *Magnetic Resonance in Medicine, 51,* 807–815. [PubMed]

Kikuta, K., Takagi, Y., Nozaki, K., Hanakawa, T., Okada, T., Miki, Y., et al. (2006). Early experience with 3-T magnetic resonance tractography in the surgery of cerebral arteriovenous malformations in and around the visual pathway. *Neurosurgery, 58,* 331–337. [PubMed]

Krolak-Salmon, P., Guenot, M., Tiliket, C., Isnard, J., Sindou, M., Mauguiere, F., et al. (2000). Anatomy of optic nerve radiations as assessed by static perimetry and MRI after tailored temporal lobectomy. *British Journal of Ophthalmology, 84,* 884–889. [PubMed] [Article]

Lazar, M., & Alexander, A. L. (2002). *White matter tractography using random vector (RAVE) perturbation*. Paper presented at the Proceedings of ISMRM Annual Meeting, Honolulu.

Leuret, F., & Gratiolet, L.-P. (1839). *Anatomie comparée du Système Nerveux. Considéré dans ses rapports avec l'Intelligence* (vol. II). Paris: J-B Baillère et fils.

Meyer, A. (1907). The connections of the occipital lobes and the present status of the cerebral visual affections. *Transactions Association of the American Physicians, 22,* 7–23.

Miller, N. R. (2005). Diffusion tensor imaging of the visual sensory pathway: Are we there yet? *American Journal of Ophthalmology, 140,* 896–897. [PubMed]

Mori, S., Crain, B. J., Chacko, V. P., & van Zijl, P. C. (1999). Three-dimensional tracking of axonal projections in the brain by magnetic resonance imaging. *Annals of Neurology, 45,* 265–269. [PubMed]

Nilsson, D., Starck, G., Ljungberg, M., Ribbelin, S., Jönsson, L., Malmgren, K., et al. (2007). Intersubject variability in the anterior extent of the optic radiation assessed by tractography. *Epilepsy Research, 77,* 11–16. [PubMed]

Okada, T., Miki, Y., Kikuta, K., Mikuni, N., Urayama, S., Fushimi, Y., et al. (2007). Diffusion tensor fiber tractography for arteriovenous malformations: Quantitative analyses to evaluate the corticospinal tract and optic radiation. *American Journal of Neuroradiology, 28,* 1107–1113. [PubMed]

Parker, G. J., Haroon, H. A., & Wheeler-Kingshott, C. A. (2003). A framework for a streamline-based probabilistic index of connectivity (PICo) using a structural interpretation of MRI diffusion measurements. *Journal of Magnetic Resonance Imaging, 18,* 242–254. [PubMed]

Peled, S., Gudbjartsson, H., Westin, C. F., Kikinis, R., & Jolesz, F. A. (1998). Magnetic resonance imaging shows orientation and asymmetry of white matter fiber tracts. *Brain Research, 780,* 27–33. [PubMed]

Peltier, J., Travers, N., Destrieux, C., & Velut, S. (2006). Optic radiations: A microsurgical anatomical study. *Journal of Neurosurgery, 105,* 294–300. [PubMed]

Perrin, M., Poupon, C., Cointepas, Y., Rieul, B., Golestani, N., Pallier, C., et al. (2005, July). Fiber tracking in q-ball fields using regularized particle trajectories. In *Proceedings of the 19th International Conference on Information Processing in Medical Imaging (IPMI '05), Glenwood Springs, CO* (pp. 52–63).

Powell, H. W., Parker, G. J., Alexander, D. C., Symms, M. R., Boulby, P. A., Wheeler-Kingshott, C. A., et al. (2005). MR tractography predicts visual field defects following temporal lobe resection. *Neurology, 65,* 596–599. [PubMed]

Rohde, G. K., Barnett, A. S., Basser, P. J., Marenco, S., & Pierpaoli, C. (2004). Comprehensive approach for correction of motion and distortion in diffusion-weighted MRI. *Magnetic Resonance in Medicine, 51,* 103–114. [PubMed]

Rohde, G. K., Barnett, A. S., Basser, P. J., & Pierpaoli, C. (2005). Estimating intensity variance due to noise in registered images: Applications to diffusion tensor MRI. *Neuroimage, 26,* 673–684. [PubMed]

Rubino, P. A., Rhoton, A. L., Jr., Tong, X., & Oliveira, E. (2005). Three-dimensional relationships of the optic radiation. *Neurosurgery, 57,* 219–227. [PubMed]

Schmahmann, J. D., & Pandya, D. N. (2006). *Fiber pathways of the brain*. New York: Oxford University Press.

Sherbondy, A., Akers, D., Mackenzie, R., Dougherty, R., & Wandell, B. (2005). Exploring connectivity of the brain's white matter with dynamic queries. *IEEE Transactions on Visualization and Computer Graphics, 11,* 419–430. [PubMed]

Sherbondy, A. J., Dougherty, R., Ben-Shachar, M., Napel, S., & Wandell, B. A. (2008). ConTrack: Finding the most likely pathways between brain regions using diffusion tractography. *Journal of Vision, 8*(9):15, 1–16, http://journalofvision.org/8/9/15/, doi:10.1167/8.9.15. [PubMed] [Article]

Sincoff, E. H., Tan, Y., & Abdulrauf, S. I. (2004). White matter fiber dissection of the optic radiations of the temporal lobe and implications for surgical approaches to the temporal horn. *Journal of Neurosurgery, 101,* 739–746. [PubMed]

Taoka, T., Sakamoto, M., Iwasaki, S., Nakagawa, H., Fukusumi, A., Hirohashi, S., et al. (2005). Diffusion tensor imaging in cases with visual field defect after anterior temporal lobectomy. *American Journal of Neuroradiology, 26,* 797–803. [PubMed] [Article]

Yamamoto, A., Miki, Y., Urayama, S., Fushimi, Y., Okada, T., Hanakawa, T., et al. (2007). Diffusion tensor fiber tractography of the optic radiation: Analysis with 6-, 12-, 40-, and 81-directional motion-probing gradients, a preliminary study. *American Journal of Neuroradiology, 28,* 92–96. [PubMed] [Article]

Yamamoto, T., Yamada, K., Nishimura, T., & Kinoshita, S. (2005). Tractography to depict three layers of visual field trajectories to the calcarine gyri. *American Journal of Neuroradiology, 140,* 781–785. [PubMed]

Yasargil, M. G., Türe, U., & Yasargil, D. C. (2004). Impact of temporal lobe surgery. *Journal of Neurosurgery, 101,* 725–738. [PubMed]

Yushkevich, P. A., Piven, J., Hazlett, H. C., Smith, R. G., Ho, S., Gee, J. C., et al. (2006). User-guided 3D active contour segmentation of anatomical structures: Significantly improved efficiency and reliability. *Neuroimage, 31,* 1116–1128. [PubMed]